Chinese Chemical Letters 33 (2022) 4930–4935

Contents lists available at ScienceDirect

Chinese Chemical Letters

journal homepage: www.elsevier.com/locate/cclet

Ruthenium-modified porous $NiCo_2O_4$ nanosheets boost overall water splitting in alkaline solution

Rui Yang[a], Xuezhao Shi[a], Yanyan Wang[b], Jing Jin[a], Hanwen Liu[a], Jie Yin[a], Yong-Qing Zhao[a], Pinxian Xi[a,*]

[a] State Key Laboratory of Applied Organic Chemistry Frontiers Science Center for Rare Isotopes College of Chemistry and Chemical Engineering, Lanzhou University Lanzhou 730000, China
[b] Lanzhou Jinchuan Advanced Materials Technology Co., Ltd., Jinchang 737100, China

ARTICLE INFO

Article history:
Received 30 August 2021
Revised 17 December 2021
Accepted 22 December 2021
Available online 27 December 2021

Keywords:
Ru modification
Porous nanosheets
Oxygen vacancy
Spinel-based oxides
Water splitting

ABSTRACT

Exploring efficient oxygen evolution reaction (OER) and hydrogen evolution reaction (HER) electrocatalysts is crucial for developing water splitting devices. The composition and structure of catalysts are of great importance for catalytic performance. In this work, a heterogeneous Ru modified strategy is engineered to improve the catalytic performance of porous $NiCo_2O_4$ nanosheets (NSs). Profiting from favorable elements composition and optimized structure property of decreased charge transfer barrier, more accessible active sites and increased oxygen vacancy concentration, the Ru-$NiCo_2O_4$ NSs exhibits excellent OER activity with a low overpotential of 230 mV to reach the current density of 10 mA/cm^2 and decent durability. Furthermore, Ru-$NiCo_2O_4$ NSs show superior HER activity than the pristine $NiCo_2O_4$ NSs, as well. When assembling Ru-$NiCo_2O_4$ NSs couple as an alkaline water electrolyzer, a cell voltage of 1.60 V can deliver the current density of 10 mA/cm^2. This work provides feasible guidance for improving the catalytic performance of spinel-based oxides.

Electrocatalytic water splitting is regarded as a technology with great prospects for production of clean hydrogen energy [1–5]. However, there still exist great challenges to fabricate exceedingly efficient catalysts to accelerate the oxygen evolution reaction (OER) and the hydrogen evolution reaction (HER) in alkaline media, due to their sluggish kinetics and unseemly thermodynamics [6–10]. Especially for OER process, it contains complicated multistep proton-coupled electron transfer processes, responsible for a large overpotential [11]. At present, the commonly recognized OER and HER catalysts with prominent performance are Ir-based and Pt-based materials, respectively [12,13]. But high price and limited reserve of these noble metals restrain their widespread application. Among all kinds of alternative catalysts for expensive materials, spinel-based oxides have gained enormous attention owing to rich element composition, variable valence state and good stability during electrocatalytic process [14–17]. Nevertheless, the electrocatalytic activity of spinel-based oxides without further modulating is still far from people's satisfaction.

Obviously, the catalytic activity of catalysts is highly associated with their elemental composition and structure traits [18,19] Introducing heteroatoms into substrate materials has been certified a useful strategy to optimize materials' surface property and improve their catalytic performance [20,21]. A critical point lies in the choice of heteroelement. It has been recorded that Ru has moderate H* and OH* intermediates absorption energy, due to the similar Ru-H bond energy (~65 kcal/mol) with Pt-H bond energy (~70 kcal/mol) and reasonable oxophilic character [22–25]. And the price of Ru is the cheapest among Pt-group metals [26]. Therefore, Ru has great potential to be used in electrocatalytic water splitting realm. For instance, Huang and co-workers reported the synthesis of Ru-doped CoCr LDHs as efficient a OER catalyst due to synergetic charge transfer [27]. Besides, Chen and co-workers designed RuCo nanoalloys catalyst, displaying impressive HER performance, with the overpotential of 28 mV being need to reach the current density of 10 mA/cm^2 [26]. More importantly, Qi and co-workers engineered Co MOF by introducing Ru, forming hollow (Ru-Co)O_x compound which can promote overall water splitting performance [28]. In addition, the morphology of catalysts also plays a pivotal role in catalytic process. The two-dimension (2D) nanomaterial with largely exposed surface atoms and edge sites is deemed as an appealing electrocatalyst for water splitting, which is not only in favor of the absorption of reactant species due to its large parts of superficial coordination-unsaturated atoms but

* Corresponding author.
E-mail address: xipx@lzu.edu.cn (P. Xi).

https://doi.org/10.1016/j.cclet.2021.12.058
1001-8417/

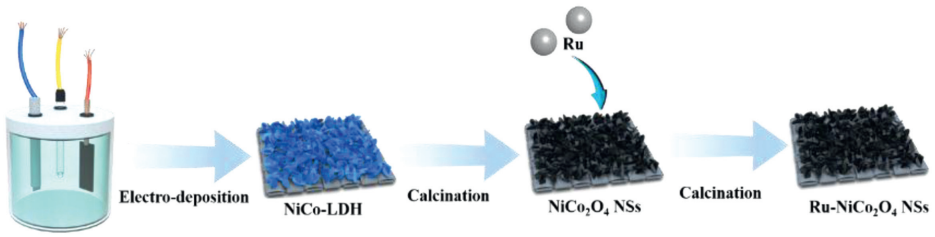

Scheme 1. Synthetic scheme of the Ru-$NiCo_2O_4$ NSs electrocatalyst.

also helpful to abridged diffusion path of reactants and products [21,29,30]. It has been reported that nanosheets array structure of various catalysts show excellent performance such as NiFe-LDH [21], CoOOH [31] and Co-NiS_2 [32]. Inspired by these relevant reports, it may be working to construct 2D spinel-based oxides catalysts integrated with Ru to achieve efficient overall water splitting.

Herein, we synthesized porous $NiCo_2O_4$ nanosheets (NSs) arrays coupled with Ru aligned on carbon fiber cloth (CFC) (denoted as Ru-$NiCo_2O_4$ NSs) through a facile impregnating method to introduce Ru. The obtained porous Ru-$NiCo_2O_4$ NSs features desirable elements composition and favorable structure virtues which showcase higher oxygen vacancy concentration, decreased charge transfer impedance and more accessible active sites. Moreover, the introduction of Ru greatly reduces the activation energy of OER process. Accordingly, Ru-$NiCo_2O_4$ NSs manifest superior OER performance with only an overpotential of 230 mV at the current density of 10 mA/cm^2 and long-term stability in alkaline media. Furthermore, Ru-$NiCo_2O_4$ NSs show superior HER activity than $NiCo_2O_4$ NSs counterpart. The integrated alkaline electrolyzer using Ru-$NiCo_2O_4$ NSs as bifunctional electrodes materials needs 1.60 V to reach the current density of 10 mA/cm^2. And the activity and durability of Ru-$NiCo_2O_4$ NSs overall water splitting system are both superior to Pt/C||RuO_2 system. This work presents a viable guide for developing efficient spinel-based oxides electrocatalysts.

The synthesis of $NiCo_2O_4$ NSs refers to the previous report [20]. Firstly, the precursor NiCo-LDH was synthesized by a facile electro-deposition method. 0.1 mol/L $Ni(NO_3)_2{\cdot}6H_2O$ (20 mL) and 0.1 mol/L $Co(NO_3)_2{\cdot}6H_2O$ (40 mL) were mixed as electrodeposition electrolyte. A piece of carbon fabric cloth (CFC) was used as electro-deposition substrate. The process was performed at −1 V (*vs*. Ag/AgCl) for 15 min. After finishing, the final product was rinsed with DI water several times, and then dried in 50 °C electro-oven. The $NiCo_2O_4$ NSs were obtained by calcining NiCo-LDH at 300 °C for 2 h with the heating rate (2 °C/min) in air atmosphere. Then, the Ru-$NiCo_2O_4$ was synthesized by impregnating $NiCo_2O_4$ NSs in $RuCl_3$ solution (10 mg/mL) for 20 min, then dried in 50 °C electro-oven and further annealed at 300 °C for 2 h in air atmosphere.

X-ray diffraction (XRD) measurement was conducted on Rigaku MiniFlex 600 diffractometer from 10° to 90° under a constant voltage of 40 kV and constant current of 15 mA. The morphology characterization was obtained by ThermoFisher Apreo S filed-emission scanning electron microscopy (FESEM) with a voltage of 30 kV. Transmission electron microscopy (TEM), high-resolution transmission electron microscopy (HR-TEM) and EDS mapping pictures of samples was collected on a Tecnai G2 F30 filed emission transmission electron microscopy. Raman spectra were measured on a Horiba LabRAM HR Evolution spectrophotometer with a laser line of 532 nm. Electron spin resonance (ESR) experiments were made on JES-FA300 electron spin resonance spectrometer. X-ray photoelectron spectroscopy (XPS) was performed by a VG ESCALAB 220I-XL device. The data were corrected using C 1s line as standard. Ultraviolet photoelectron spectrometer (UPS) was conducted on Kratos Axis Supra device. The contact angle test was carried out on a Kruss DSA100 optical contact angle/surface tension meter.

Electrochemical measurements were performed on CHI 760E electrochemical workstation (Shanghai Chenhua Instrument Corp., China) with a standard three-electrode configuration, with Pt plate and Hg/HgO as counter electrode and reference electrode, respectively, for OER test. While for HER test, the counter electrode was changed to a carbon rod. The catalysts grown on CFC were used as working electrodes directly. 1.0 mol/L KOH solution was used as electrolyte and Linear scan voltammogram (LSV) curves were carried out at a scan rate of 2 mV/s. All the electrode potential was converted to the reversible hydrogen electrode (RHE), using the equation $E_{RHE} = E_{Hg/HgO} + 0.0591 \times pH + 0.098$ V.

Scheme 1 illustrates the synthesis procedure of catalysts. At first, the phases of samples obtained were analyzed by the X-ray diffraction (XRD) technique. Fig. 1a shows that the diffraction peaks of the pristine $NiCo_2O_4$ NSs can well match with cubic $NiCo_2O_4$ (JCPDS No. 20–781, space group F*3). And the Ru-$NiCo_2O_4$ NSs possess similar diffraction patterns with the pristine $NiCo_2O_4$ NSs without related Ru oxides phase being detected, implying Ru was doped successfully in $NiCo_2O_4$ NSs preliminarily. As shown in Fig. 1b and Fig. S1a (Supporting information), the original $NiCo_2O_4$ NSs presents interlaced nanosheets morphology grown on CFC characterized by scanning electron microscope (SEM). From the transmission electron microscope (TEM) image (Fig. 1c), it can be detected that the nanosheets present porous property. It can be seen from Figs. 1d and e and Fig. S1b (Supporting information), the Ru-$NiCo_2O_4$ NSs exhibit similar morphology feature with the pristine $NiCo_2O_4$ NSs, declaring the introducing of Ru does not ruin porous nanosheets structure of $NiCo_2O_4$ NSs. It has been documented that porous structure is in favor of accelerating mass transfer process and enhancing the accessibility of active sites [33–35]. Furthermore, high-resolution transmission electron microscopy (HRTEM) image of Ru-$NiCo_2O_4$ NSs exhibits lattice spacing of 0.24 nm, which can be assigned to (311) plane of $NiCo_2O_4$ (Fig. 1f). The high-angle annular dark-field scanning TEM image (Fig. 1g) and TEM energy-dispersive spectra (EDS) mapping images (Fig. 1h) show the uniform distribution of Ru, Ni, Co and O in the checked region. Furthermore, Fig. 1i presents the crystal structure of $NiCo_2O_4$.

Moreover, the X-ray photoelectron spectroscopy (XPS), Ultraviolet photoelectron spectrometer (UPS), Raman spectra and electron spin-resonance spectroscopy (ESR) were carried out to further probe the structural information of catalysts obtained. As shown in XPS survey spectrums of Ru-$NiCo_2O_4$ NSs and $NiCo_2O_4$ NSs (Fig. S2 in Supporting information), the Ru 3p signal lays in Ru-$NiCo_2O_4$ NSs, while it does not appear in $NiCo_2O_4$ NSs, confirming Ru was introduced into $NiCo_2O_4$ NSs matrix successfully, which is consistent with the TEM-EDS result. The high-resolution O1s XPS spectra (Fig. 2a) can be deconvoluted into three parts: lattice oxygen, oxygen vacancy, or hydroxyl group and absorbed oxygen from low binding energy to high binding energy in sequence [36,37] Compared with $NiCo_2O_4$ NSs, the binding energy of O 1s XPS spectra

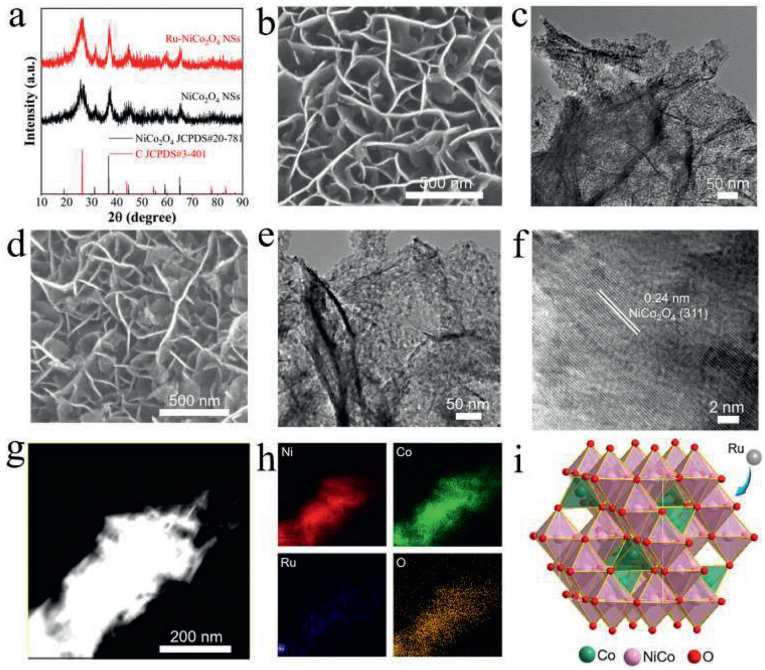

Fig. 1. (a) XRD pattern of $NiCo_2O_4$ and Ru-$NiCo_2O_4$ NSs. (b, c) SEM, TEM images of $NiCo_2O_4$ NSs. (d) SEM, (e) TEM and (f) HRTEM of Ru-$NiCo_2O_4$ NSs. (g, h) HAADF-STEM image and corresponding elemental mapping images of Ru-$NiCo_2O_4$ NSs. (i) Crystal structure of $NiCo_2O_4$.

for Ru-$NiCo_2O_4$ NSs positively shifts ~0.2 eV, exhibiting a slight electron-deficiency O state. Furthermore, the binding energy of Ru $3p_{3/2}$ in Ru-$NiCo_2O_4$ NSs is 463.7 eV (Fig. 2b), which is located between the reference samples $RuCl_3$ (Ru^{3+}) and RuO_2 (Ru^{4+}), implying that the average valence state of Ru is between +3 and +4 in Ru-$NiCo_2O_4$ NSs [27,38]. Besides, there is no distinct difference between $NiCo_2O_4$ NSs and Ru-$NiCo_2O_4$ NSs concerning Co and Ni 2p XPS spectra, affirming the preservation of $NiCo_2O_4$ phase after Ru modification (Fig. S3 in Supporting information). In addition, the UPS was conducted to probe dynamics of electrons on the surface of the as-prepared catalysts [39]. As shown in Fig. 2c, the Ru-$NiCo_2O_4$ NSs and $NiCo_2O_4$ NSs exhibit different secondary electron cutoff energy with 16.34 eV for Ru-$NiCo_2O_4$ NSs and 16.22 eV for $NiCo_2O_4$ NSs and thus the corresponding work function are 4.88 eV and 5.00 eV for Ru-$NiCo_2O_4$ NSs and $NiCo_2O_4$ NSs, respectively. The smaller work function indicates that Ru modulation facilitates the electronic properties of Ru-$NiCo_2O_4$ NSs, which is contributed to enhancing catalytic activity [40]. Besides, Raman as a surface-sensitive spectrum technology was further applied to gain insights into $NiCo_2O_4$ NSs before and after Ru modification. As shown in Fig. 2d, the Ru-$NiCo_2O_4$ NSs showcases similar spectra patterns with the pristine $NiCo_2O_4$ NSs except for a slight blue shift, which is due to the doping of Ru. Furthermore, the Raman spectra of Ru-$NiCo_2O_4$ NSs exhibit different spectra feature compared with RuO_2 (Fig. S4 in Supporting information), which implies the Ru may exist as a highly dispersed state in $NiCo_2O_4$ NSs substrate and further indicating that Ru are doped into $NiCo_2O_4$ NSs successfully. Moreover, ESR spectra were conducted to investigate the change of oxygen vacancy. From Fig. 2e, it can be seen that Ru-$NiCo_2O_4$ NSs owns a stronger ESR signal originating from the electron trapped at oxygen vacancies than that of $NiCo_2O_4$ counterpart [41,42]. Therefore, we can deduce that the Ru-$NiCo_2O_4$ NSs possess more oxygen vacancies than $NiCo_2O_4$ NSs, which is helpful to facilitate water dissociation [43]. Furthermore, the excellent hydrophilicity feature of Ru-$NiCo_2O_4$ NSs supported on CFC enables the easy accessibility of reactants and fast release of product molecules, thus accelerating catalytic process (Fig. 2f, the inset shows the contact angle of bare CFC) [44].

The electrocatalytic performance of catalysts prepared was evaluated by a standard three-electrode configuration using 1.0 mol/L KOH as electrolyte. Linear scan voltammogram (LSV) curves of OER (Fig. 3a) show that the required overpotentials for Ru-$NiCo_2O_4$ NSs, $NiCo_2O_4$ NSs and RuO_2 to reach the current density of 10 mA/cm^2 are 230 mV, 340 mV and 329 mV, respectively, manifesting excellent OER activity of Ru-$NiCo_2O_4$ NSs. Furthermore, the Fig. 3b illustrates Ru-$NiCo_2O_4$ NSs possesses a small Tafel slope (79 mV/dec) lower than that of $NiCo_2O_4$ NSs (95 mV/dec) and RuO_2 (82 mV/dec) counterparts, indicating the accelerated OER kinetic for Ru-$NiCo_2O_4$ NSs. Besides, the stability is also a vital aspect for assessing the performance of catalysts. From Fig. 3g (green line), it can be seen that Ru-$NiCo_2O_4$ NSs show nearly no activity decay in the period of 42 h OER test. To gain the insights about the origin of activity, the electrochemical impedance spectroscopy (EIS) of Ru-$NiCo_2O_4$ NSs and $NiCo_2O_4$ NSs were collected to investigate charge transfer ability. As shown in Fig. 3c, Ru-$NiCo_2O_4$ NSs exhibits a smaller radius than that of $NiCo_2O_4$ NSs counterpart, implying a lower charge transfer (R_{ct}) impedance of Ru-$NiCo_2O_4$ NSs for OER process, which is conducive to improving OER performance [45]. In addition, electrochemical double-layer capacitance (C_{dl}) was tested to access the electrochemical surface area (ECSA) of the as-prepared catalysts (Fig. S5 in Supporting information) [46]. The value of C_{dl} for Ru-$NiCo_2O_4$ NSs and $NiCo_2O_4$ NSs are 278 mF/cm^2 and 200 mF/cm^2 (Fig. 3h), respectively, suggesting the larger ECSA of Ru-$NiCo_2O_4$ NSs. The larger ECSA manifests more accessible active sites on Ru-$NiCo_2O_4$ NSs surface in catalytic process, thus boosting OER performance. Moreover, LSV curves at various temperature for Ru-$NiCo_2O_4$ NSs and $NiCo_2O_4$ NSs were analyzed to evaluate apparent kinetic barriers in OER process. Extended the obtained Arrhenius plots to the OER thermodynamic equilibrium potential, the value of apparent activation energy (E_a) can be obtained [47,48]. As illustrated in Fig. S6 (Supporting information), the value of E_a of Ru-$NiCo_2O_4$ NSs is 26.6 kJ/mol while the E_a of $NiCo_2O_4$ NSs is 45.9 kJ/mol, implying Ru modification availably decrease E_a for OER course.

Due to the similar Ru-H bond energy to Pt-H bond energy [22], the HER performance of $NiCo_2O_4$ NSs after Ru modification may

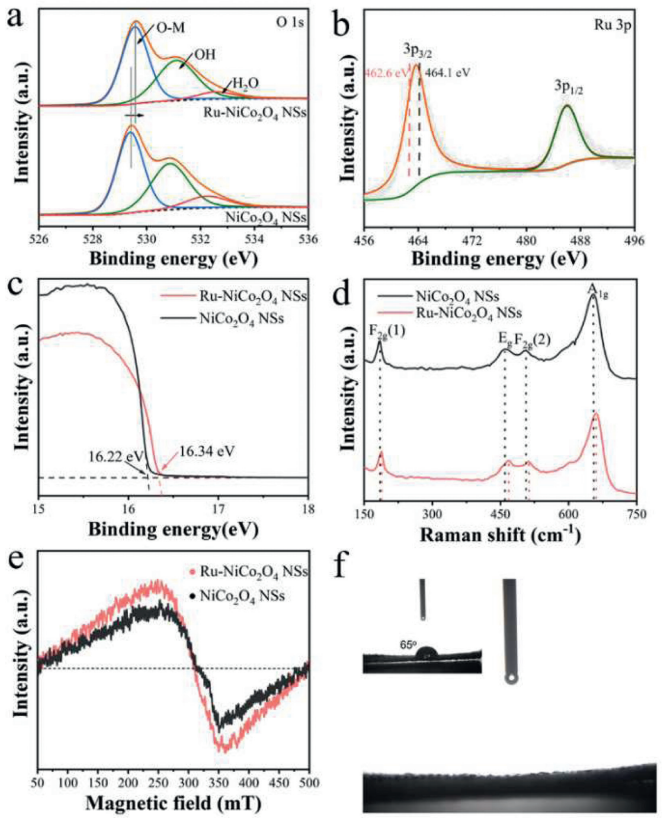

Fig. 2. (a) O 1s spectra of Ru-$NiCo_2O_4$ NSs and $NiCo_2O_4$ NSs. (b) Ru 3p spectra of Ru-$NiCo_2O_4$ NSs. (c) UPS spectra (d) Raman spectra and (e) ESR spectra of Ru-$NiCo_2O_4$ NSs and $NiCo_2O_4$ NSs. (f) Contact angle of water droplets on the surface of Ru-$NiCo_2O_4$ NSs and bare CFC (inset).

also be improved. As shown in LSV curves of HER (Fig. 3d), an overpotential of 313 mV is needed for $NiCo_2O_4$ NSs to reach current density of 10 mA/cm^2, while the value decreases to 117 mV for Ru-$NiCo_2O_4$ NSs. The Tafel slopes are analyzed to be 88 mV/dec and 97 mV/dec for Ru-$NiCo_2O_4$ NSs and $NiCo_2O_4$ NSs, respectively (Fig. 3e), declaring a more favorable HER kinetics for Ru-$NiCo_2O_4$ NSs. Regarding long-time stability, the chronopotentiometry test shows no obvious activity degradation of Ru-$NiCo_2O_4$ NSs after 42 h (Fig. 3g, blue line). Furthermore, EIS plots were collected to assess charge transfer feature of materials between electrode and electrolyte interface. As illustrated in Fig. 3f, the Ru-$NiCo_2O_4$ NSs possess a smaller R_{ct} than that of $NiCo_2O_4$ NSs, manifesting that Ru modification accelerates charge transfer in HER process, thus promoting HER activity. Fig. 3i displays a larger C_{dl} for Ru-$NiCo_2O_4$ NSs (21.3 mF/cm^2) than $NiCo_2O_4$ NSs (2.2 mF/cm^2) based on CVs test (Fig. S7 in Supporting information), thereby a larger ECSA of Ru-$NiCo_2O_4$ NSs for HER catalysis, which is also favorable to promote HER performance.

In situ Raman spectra characterization analysis was performed to reveal changes on Ru-$NiCo_2O_4$ NSs electrodes during the OER and HER processes. The peak located at ~470 cm^{-1} and ~670 cm^{-1} are attributed to E_g phonon modes and A_{1g} phonon modes of Ru-$NiCo_2O_4$ NSs, respectively (Fig. 4). Potentials from open circuit voltage (OCV) to 1.6 V *vs.* RHE were applied for OER in suit Raman measurements. The corresponding spectra result are shown in Fig. 4a, characteristic peaks associated with E_g and A_{1g} phonon modes exhibits no differentiable variation, implying good stability of Ru-$NiCo_2O_4$ NSs in OER process. For HER, we applied potential from OCV to −0.25 V *vs.* RHE. The corresponding spectra (Fig. 4b) obtained also show no obvious change, manifesting good HER stability of Ru-$NiCo_2O_4$ NSs. Besides, SEM characterization was conducted to probe the change of morphology of Ru-$NiCo_2O_4$ NSs after OER and HER. As shown in Fig. S8 (Supporting information), the morphology of Ru-$NiCo_2O_4$ NSs after OER and HER remains

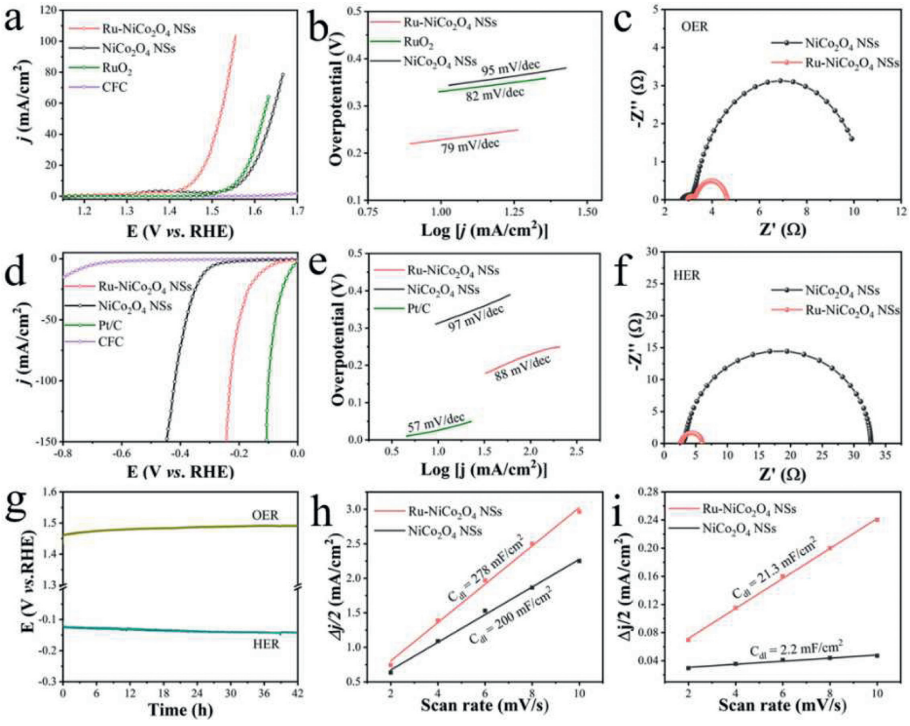

Fig. 3. Electrochemical performance for OER and HER. (a) LSV curves and (b) the corresponding Tafel plots of Ru-$NiCo_2O_4$ NSs, $NiCo_2O_4$ NSs and RuO_2 for OER., (c) EIS of Ru-$NiCo_2O_4$ NSs and $NiCo_2O_4$ NSs for OER. (d) LSV curves and (e) the corresponding Tafel plots of Ru-$NiCo_2O_4$ NSs, $NiCo_2O_4$ NSs and Pt/C for HER. (f) EIS of Ru-$NiCo_2O_4$ NSs and $NiCo_2O_4$ NSs for HER. (g) Chronopotentiometry test of Ru-$NiCo_2O_4$ NSs for OER and HER at 10 mA/cm^2. (h, i) Capacitive currents of Ru-$NiCo_2O_4$ NSs and $NiCo_2O_4$ NSs with different scan rates for OER and HER, respectively.

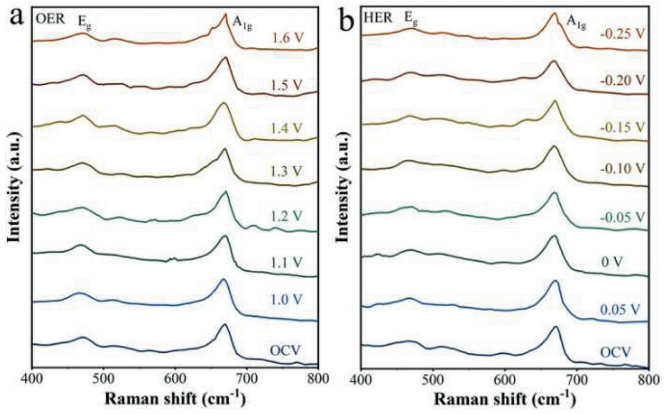

Fig. 4. *In situ* Raman spectra of Ru-$NiCo_2O_4$ NSs during (a) OER and (b) HER.

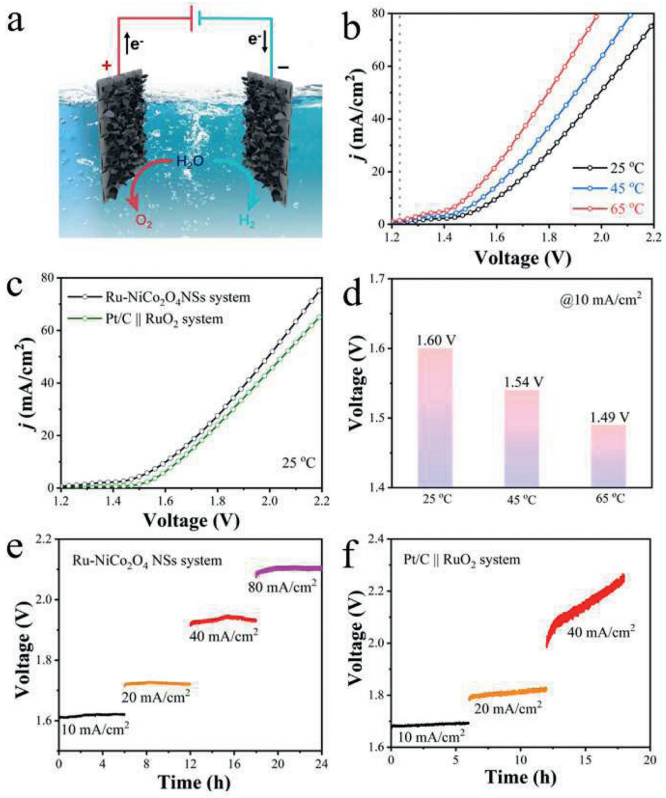

Fig. 5. (a) Schematic illustration of the configuration of alkaline overall water splitting device. (b) LSV curves for overall water splitting applying Ru-$NiCo_2O_4$ NSs as both cathode and anode at different temperatures. (c) LSV polarization curves of Ru-$NiCo_2O_4$ NSs system and Pt/C||RuO_2 system for overall water splitting at 25 °C. (d) Comparison of the cell voltages to reach the current density of 10 mA/cm^2 of Ru-$NiCo_2O_4$ NSs system at various temperatures., (e, f) Long-term stability test of overall water splitting at various current density of 10, 20, 40 and 80 mA/cm^2 for Ru-$NiCo_2O_4$ NSs system and Pt/C||RuO_2 system, respectively.

nanosheets structure. All evidences illustrate the good stability of Ru-$NiCo_2O_4$ NSs.

Based on the enhanced OER and HER performance of Ru-$NiCo_2O_4$ NSs, the overall water-splitting performance was assessed by utilizing Ru-$NiCo_2O_4$ NSs as both anode and cathode catalysts in 1.0 mol/L KOH solution. Fig. 5a illustrates the configuration of overall water splitting device. Fig. 5b showcases the LSV curves of Ru-$NiCo_2O_4$ NSs for the overall water splitting at various temperatures (25, 45 and 65 °C). A cell voltage of 1.60 V was needed to reach the current density of 10 mA/cm^2 at 25 °C for Ru-$NiCo_2O_4$ NSs couple, which is lower than that of Pt/C||RuO_2 set (1.64 V) (Fig. 5c). The overall water splitting performance of Ru-$NiCo_2O_4$ NSs system can be further improve by increasing temperature. As exhibited in Fig. 5d, cell voltages needed to obtain the current density of 10 mA/cm^2 at 45 °C and 65 °C are 1.54 V and 1.49 V, respectively. In addition, Ru-$NiCo_2O_4$ NSs set displays good stability on a long-time testing at different current densities 10, 20, 40, 80 mA/cm^2 (Fig. 5e), while for Pt/C||RuO_2 system, the cell voltages enlarge constantly over time (Fig. 5f). All the results verify Ru-$NiCo_2O_4$ NSs can be used as efficient overall water splitting catalysts.

In summary, the porous $NiCo_2O_4$ NSs integrated with Ru through a facile impregnation method is devised. The obtained Ru-$NiCo_2O_4$ NSs catalysts exhibit superior OER activity with a low overpotential of 230 mV at 10 mA/cm^2, the enhanced HER activity and robust stability. The promotion of catalytic performance of Ru-$NiCo_2O_4$ NSs can be attributed to the low charge transfer impedance, more accessible active sites and higher oxygen vacancy concentration. Experimental results demonstrate that the introduction of Ru efficiently regulates the surface structure property of $NiCo_2O_4$ NSs. The optimized components and structural advantages facilitate synergistically OER and HER process. This work presents a practicable strategy for improving the catalytic performance of spine-based oxides for both OER and HER.

Declaration of competing interest

The authors declare that they have no known competing financial interests or personal relationships that could have appeared to influence the work reported in this paper.

Acknowledgments

We acknowledge support from the National Natural Science Foundation of China (Nos. 21922105 and 21931001), the National Key R&D Program of China (2021YFA1501101) as well as the Special Fund Project of Guiding Scientific and Technological Innovation Development of Gansu Province (No. 2019ZX-04) and the 111 Project (No. B20027). We also acknowledge support by the Fundamental Research Funds for the Central Universities (Nos. lzujbky-2021-pd04, lzujbky-2021-sp41, lzujbky-2021-it12 and lzujbky-2021-37). J. Yin acknowledges the support of the China Postdoctoral Science Foundation (No. 2021M691375) and the China National Postdoctoral Program for Innovative Talents (No. BX20200157).

Supplementary materials

Supplementary material associated with this article can be found, in the online version, at doi:10.1016/j.cclet.2021.12.058.

References

[1] Z.W. Seh, J. Kibsgaard, C.F. Dickens, et al., Science 355 (2017) eaad4998.
[2] I. Roger, M.A. Shipman, M.D. Symes, et al., Nat. Rev. Chem. 1 (2017) 0003.
[3] H. Sun, L. Chen, Y. Lian, et al., Adv. Mater. 32 (2020) 2006784.
[4] J. Cao, C. Lei, J. Yang, et al., J. Mater. Chem. A 6 (2018) 18877.
[5] K. Wang, Wang X, Li Z, et al., Nano Energy 77 (2020) 105162.
[6] L. An, J. Feng, Y. Zhang, et al., Adv. Funct. Mater. 29 (2019) 1805298.
[7] L. Wang, Z. Li, K. Wang, et al., Nano Energy 74 (2020) 104850.
[8] C. Lei, S. Lyu, J. Si, et al., ChemCatChem 11 (2019) 5855–5874.
[9] F. Cheng, L. Wang, H. Wang, et al., Nano Energy 71 (2020) 104621.
[10] C. Liu, J. Qian, Y. Ye, et al., Nat. Catal. 4 (2021) 36–45.
[11] S.L. Zhang, B.Y. Guan, X.F. Lu, et al., Adv. Mater. 32 (2020) 2002235.
[12] T. Wu, S. Sheng, J. Song, et al., Nat Catal. 2 (2019) 763–772.
[13] J. Kim, H. Jung, S.M. Jung, et al., J. Am. Chem. Soc. 143 (2021) 1399–1408.
[14] Q. Zhao, Z. Yan, C. Chen, et al., Chem. Rev. 117 (2017) 10121–10211.
[15] J. Li, D. Chu, H. Dong, et al., J. Am. Chem. Soc. 142 (2020) 50–54.
[16] J. Bao, X. Zhang, B. Fan, et al., Angew. Chem. Int. Ed. 54 (2015) 7399–7404.
[17] Y. Sun, H. Liao, J. Wang, et al., Nat Catal. 3 (2020) 554–563.
[18] Y. Duan, J.Y. Lee, S. Xi, et al., Angew. Chem., Int. Ed. 60 (2021) 7418–7425.
[19] Y. Wen, P. Chen, L. Wang, et al., J. Am. Chem. Soc. 143 (2021) 6482–6490.
[20] J. Yin, J. Jin, M. Lu, et al., J. Am. Chem. Soc. 142 (2020) 18378–18386.
[21] R. Yang, L. An, Y. Zhang, et al., ChemCatChem 11 (2019) 6002–6007.

[22] J. Yang, B. Chen, X. Liu, et al., Angew. Chem. Int. Ed. 57 (2018) 9495–9500.
[23] X. Wang, Y. Zheng, W. Sheng, et al., Mater. Today 36 (2020) 125–138.
[24] X. Liu, F. Liu, J. Yu, et al., Adv. Sci. 7 (2020) 2001526.
[25] S.Y. Bae, J. Mahmood, I.Y. Jeon, et al., Nanoscale Horiz. 5 (2020) 43–56.
[26] J. Su, Y. Yang, G. Xia, et al., Nat. Commun. 8 (2017) 14969.
[27] C. Dong, X. Zhang, J. Xu, et al., Small 16 (2020) 1905328.
[28] C. Wang, L. Qin, Angew. Chem. Int. Ed. 59 (2020) 17219–17224.
[29] S. Jiang, R. Zhang, H. Liu, et al., J. Am. Chem. Soc. 142 (2020) 6461–6466.
[30] Q. Lu, Y. Yu, Q. Ma, et al., Adv. Mater. 28 (2016) 1917–1933.
[31] S.H. Ye, Z.X. Shi, J.X. Feng, et al., Angew. Chem. Int. Ed. 57 (2018) 2672–2676.
[32] J. Yin, J. Jin, H. Zhang, et al., Angew. Chem. Int. Ed. 58 (2019) 18676–18682.
[33] Y. Gu, A. Wu, Y. Jiao, et al., Angew. Chem. Int. Ed. 60 (2021) 6673–6681.
[34] J. Yin, J. Jin, H. Liu, et al., Adv. Mater. 32 (2020) 2001651.
[35] T.X. Nguyen, Y.C. Liao, C.C. Lin, et al., Adv. Funct. Mater. 31 (2021) 2101632.
[36] T. Zhao, X. Shen, Y. Wang, et al., Adv. Funct. Mater. 31 (2021) 2100614.
[37] J. Gao, C.Q. Xu, S.F. Hung, et al., J. Am. Chem. Soc. 141 (2019) 3014–3023.
[38] D.J. Morgan, Surface Interf. Anal. 47 (2015) 1072–1079.
[39] J. Yang, C. Wang, H. Ju, et al., Adv. Funct. Mater. 27 (2017) 1703864.
[40] Y. Duan, Z.Y. Yu, S.J. Hu, et al., Angew. Chem. Int. Ed. 58 (2019) 15772–15777.
[41] F. Lei, Y. Sun, K. Liu, et al., J. Am. Chem. Soc. 136 (2014) 6826–6829.
[42] Y. Li, M. Wen, Y. Wang, et al., Angew. Chem. Int. Ed. 60 (2021) 910–916.
[43] T. Ling, D.Y. Yan, H. Wang, et al., Nat. Commun. 8 (2017) 1509.
[44] J. Deng, H. Li, S. Wang, et al., Nat. Commun. 8 (2017) 14430.
[45] X. Ren, C. Wei, Y. Sun, et al., Adv. Mater. 32 (2020) 2001292.
[46] L. Zhang, W. Cai, N. Bao, et al., Adv. Mater. 33 (2021) 2100745.
[47] Y. Shi, J. Wang, C. Wang, et al., J. Am. Chem. Soc. 137 (2015) 7365–7370.
[48] Y. Guo, Y. Tong, P. Chen, et al., Adv. Mater. 27 (2015) 5989–5994.